



Tabletop x-ray ghost imaging with ultra-low radiation

AI-XIN ZHANG,^{1,2,†} YU-HANG HE,^{1,2,†} LING-AN WU,^{1,2,4} LI-MING CHEN,^{1,2,3,5} AND BING-BING WANG^{1,2}

¹Institute of Physics, Chinese Academy of Sciences, Beijing 100191, China

²University of Chinese Academy of Sciences, Beijing 100049, China

³CICIFSA and Department of Physics and Astronomy, Shanghai Jiao Tong University, Shanghai 200240, China

⁴e-mail: wula@aphy.iphy.ac.cn

⁵e-mail: lmchen@aphy.iphy.ac.cn

Received 9 October 2017; revised 27 February 2018; accepted 27 February 2018 (Doc. ID 306676); published 28 March 2018

Computational ghost imaging, in which an image is retrieved from a known patterned field that illuminates an object and the total transmitted intensity therefrom, has seen great advances on account of its advantages and potential applications at all wavelengths. However, even though lensless x-ray ghost imaging was anticipated more than a decade ago, its development has been hampered due to the lack of suitable optics. The image quality is proportional to the total flux in conventional projection x-ray imaging, but high photon energy could severely damage the object being imaged, so decreasing the radiation dose while maintaining image quality is a fundamental problem. Using a simple tabletop x-ray source, we have successfully realized ghost imaging of planar and natural objects with a much higher contrast-to-noise ratio compared to projection x-ray imaging at the same low-radiation dose. Ultra-low-flux imaging has been achieved, and thus radiation damage of biological specimens could be greatly reduced with this new technique. © 2018 Optical Society of America under the terms of the OSA Open Access Publishing Agreement

OCIS codes: (110.1758) Computational imaging; (340.7440) X-ray imaging; (110.0110) Imaging systems; (110.6150) Speckle imaging.

<https://doi.org/10.1364/OPTICA.5.000374>

The use of x-ray imaging in clinical medicine, crystallography, and many other research fields is extensive. Perhaps the most well-known application is x-ray radiography, based on x-ray absorption, phase contrast, coherent diffraction, and so on, which in its various forms is still the most widely used form of diagnosis and analysis. Image quality is generally proportional to the total flux, but prolonged exposure to high-photon-energy radiation can cause radiation damage in an object, especially biological organisms. The damage is proportional to the dose received, so there is a tradeoff between image quality and safety. In conventional projection imaging, the minimum illumination required for a clear image is complex. Most x-ray imaging is performed with indirect detectors based on scintillators, which absorb x-rays and emit visible light. The number of photons that reach the detector is proportional to

the incident x-ray flux, as it depends on the x-ray wavelength, scintillator thickness, visible optic coupling, etc. On the other hand, direct detectors do not need a scintillator and thus have greater sensitivity, which is determined mainly by the chip material and thickness. A recent publication has reported that direct x-ray imaging devices are capable of detecting single photons [1]. In this Letter, we report another way of realizing high-quality x-ray images with ultra-low radiation by means of “ghost” imaging.

Ghost imaging (GI) [2–5] is an indirect imaging technology, based on intensity correlation, which can retrieve the spatial information of an object with a non-spatial bucket detector if we know the distribution of the field incident on the object. This bucket detector (or single-pixel detector) is used to collect all the light transmitted or reflected from the object. The first GI experiment was performed with entangled photon pairs produced by parametric down-conversion, so the field distribution of the object signal beam was inferred from the correlated idler beam, but this requires a spatially resolving detector in the latter beam [2]. In GI experiments with classical thermal light, the field at the object may be measured with the aid of a beamsplitter, again with one beam passing to the object and the other to a reference detector with spatial resolution [3]. In fact, the beamsplitter and reference detector may both be dispensed with and replaced by a spatially patterned beam produced by a computer-controlled digital micromirror device (DMD) or spatial light modulator. Different variations of correlated imaging are known as computational GI [4,5], single-pixel imaging [6], dual photography [7], and structured illumination imaging [8]. The great interest in GI stems from the fact that, compared with conventional photography, images can have higher resolution beyond the Rayleigh diffraction limit [9] or be obtained even in poor illumination [10] or turbulent atmosphere [11]. Thus, GI has many potential applications ranging from microscopy [12–14] to three-dimensional GI [15] to long distance lidar [16,17].

In theory, GI is applicable to any wavelength, and has been recently demonstrated with x-rays [18–20] and even atoms [21]. There is immense potential for x-ray GI (XGI) in many fields, but previously the main stumbling block was that no suitable beamsplitter could be found. Yu *et al.* [18] solved this problem simply by shuttling the sample in and out of a relatively

stable, pseudo-coherent x-ray beam; Pelliccia *et al.* [19] used a crystal to diffract out the object and reference beams, which however suffered from anti-correlated instabilities due to vibrations of the crystal stage. Both groups performed their experiments at a synchrotron facility and had to add a monochromator to reduce the hard x-ray bandwidth. This year, XGI was realized with a rotating anode x-ray diffraction system as the radiation source [20]. In this case, pseudo-thermal light was generated by passing the beam through a monochromator and then through a rotating sheet of copy paper; beam splitting was again realized through crystal diffraction.

In our experiment, we pre-record a series of pseudo-thermal fields to act as the reference signal for XGI, thus the beamsplitter can be omitted; this is similar in principle to computational GI with visible light. Unlike the setup in [18], we can realize XGI of any object with the same reference signal once the pseudo-thermal fields are pre-recorded. Another advantage of our setup is that the exposure times for the reference and bucket signals can be different. The exposure time for the former can be as long as possible to obtain a clear image without having to worry about radiation damage, while it can be as short as possible for the bucket signal to avoid damaging the object so long as the detector is sensitive enough. Thus, we have succeeded in obtaining high-quality XGI images under ultra-low x-ray illuminance, even at quasi-single-photon levels.

The pseudo-thermal light is generated by an incoherent tabletop source which emits polychromatic x-rays, with a sheet of rotating sandpaper as the modulator instead of a rotating ground glass plate or DMD, which are ineffective for x-rays. Sandpaper with silicon carbide grains was used for x-ray modulation based on interference of the randomly scattered radiation [22–24], but this requires spatial coherence and a monochromatic source. In our case, “speckles” can be produced like projected shadows due to absorption. This has been exploited for x-ray imaging based on speckles generated by absorption with abrasive paper [25]. It should be emphasized that these “speckles” are not the laser interference speckles currently associated with the term, but are actually the transmitted light areas of the projected image of the sandpaper. However, for convenience we will call them speckles in this Letter. Here, their character is not determined by the beam size and monochromaticity of the source, but by the size and transmission of the SiC grains. The former influences the size of the speckles, while the latter determines their contrast. Therefore, in our experiment there is no need to use a monochromator or pinhole to improve the monochromaticity or spatial coherence of the beam, which makes the setup much simpler.

The experimental scheme is shown in Fig. 1. The x-ray source is a copper anode Incoatec I μ S stand-alone generator, operating at 40 kV and 800 μ A, and emitting characteristic wavelengths of 0.15 and 0.14 nm (photon energies of 8.04 and 8.90 keV, respectively). A Cu plate aperture blocks the unwanted beams, passing only the direct output beam, which has a fairly uniform square profile. About 27 cm downstream, the beam traverses a 20 cm diameter circular sheet of SiC sandpaper. The average size of the grains is 40 μ m, with a transmissivity of \sim 50%, thus the depth of the speckle modulation is \sim 100:50. Since the beam diverges only slightly, the distance from the sandpaper to the object had to be 2.2 m, projecting an approximately 5×5 mm² square beam, to cover the whole sample. The average size of the transmitted bright speckle on this plane was 0.4 mm. The photon flux

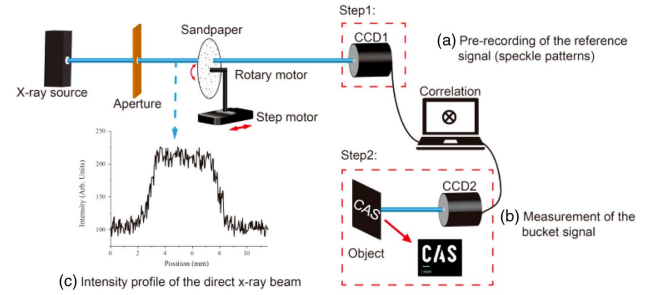


Fig. 1. Experimental scheme. (a) The reference speckle patterns are pre-recorded with CCD1. (b) The field transmitted by the object is then recorded by bucket detector CCD1/CCD2; the object and CCD1 are in the same plane. (c) Profile of the direct x-ray beam.

at the object was measured to be $\sim 2.9 \times 10^5$ photons/s \cdot mm². The sandpaper was mounted on a rotary motor fixed on a step motor, and was rotated in intervals of 0.4° – 0.9° for every 0.5 mm horizontal translation. An indirect imaging camera CCD1 (Photonic Science Large Area VHR22M_125, pixel size 25 μ m, 250 μ m thick CsI scintillator) was placed exactly in the object plane; each speckle pattern was exposed for 10 s. A total of more than 10,000 frames were recorded and stored for future use.

The camera was then replaced by the object at the same position. Another x-ray camera was placed 10 cm behind the object to measure the bucket signal; this distance is inconsequential so long as the entire beam can be collected. The sandpaper was rotated and translated in exactly the same sequence as before, and the total intensity transmitted through the object integrated for each exposure after each step of the motor. In practice, we also used a direct imaging camera CCD2 of much higher sensitivity so that very low fluxes could be detected.

Of course, it is important to check if the speckle pattern remains the same when the step motor returns to the same position every time. This depends on the stability and uniformity of the x-ray source, as well as on the precision of the step motor. To check the uniformity of the output beam, we measured the intensity profile of the direct beam using CCD1, as shown in Fig. 1(c). The plot looks rather noisy, but we can see that there are fluctuations even outside the beam cross-section, indicating that the noise is due to the CCD electronics and not fluctuations of the source (the zero intensity line is biased at 100 by the CCD software to compensate for this instrumental noise). The constancy of the speckle patterns was also checked: Fig. 2(a) shows the first pattern I_1 in the pre-recorded series of reference signals, while Fig. 2(b) is the first pattern I'_1 in the second series used to illuminate the object. The two patterns have slightly different gray scales because of the varying background noise of the CCD, but otherwise they are the same. This indicates that our pre-recording scheme is practical and feasible for XGI. The similarity of the two speckle series can also be verified by calculating the correlation coefficient defined by the following, given by the Matlab function corr2:

$$\text{corr} = \frac{\sum_x \sum_y (I(x, y) - \bar{I})(I'(x, y) - \bar{I}')}{\sqrt{\left(\sum_x \sum_y (I(x, y) - \bar{I})^2\right) \left(\sum_x \sum_y (I'(x, y) - \bar{I}')^2\right)}} \quad (1)$$

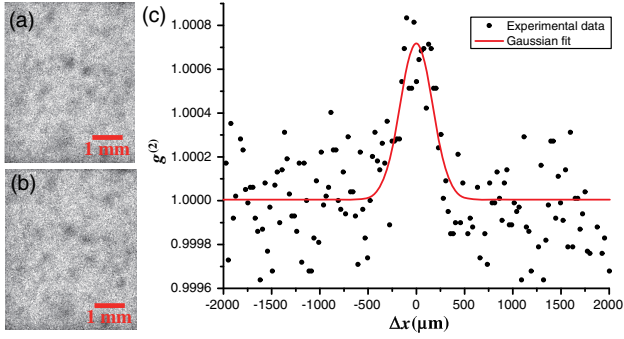


Fig. 2. (a) Pre-recorded speckle pattern I_1 . (b) Speckle pattern I'_1 in the second series of positions. (c) Second-order correlation $g^{(2)}$ as a function of distance. Black dots, experimental data; solid curve, Gaussian fit.

where $I(x, y)$ and $I'(x, y)$ represent two corresponding speckle patterns in different series, and x, y are the coordinates of the patterns. The average correlation coefficient is 0.82 for 200 measurements, which shows that our motor drive is quite good.

To verify the feasibility of our scheme and the precision of the motor drive more quantitatively, as well as characterize the nature of the pseudo-thermal light, i.e., the speckle field, a Hanbury Brown–Twiss experiment was performed with two runs of speckle patterns. The second-order correlation $g^{(2)}(x_0, y_0; x, y)$ was measured with 200 measurements using

$$g^{(2)}(x_0, y_0; x, y) = \frac{\langle I(x_0, y_0)I'(x, y) \rangle}{\langle I(x_0, y_0) \rangle \langle I'(x, y) \rangle}, \quad (2)$$

where $I(x_0, y_0)$ and $I'(x, y)$ represent the intensities at positions (x_0, y_0) and (x, y) of two series of speckle patterns.

The intensities at a fixed pixel point (x_0, y_0) on CCD1 are convoluted with those of the other series of speckles at (x, y_0) for each position of the sandpaper. The $g^{(2)}(x_0, y_0; x, y_0)$ value versus $x = x - x_0$ is plotted in Fig. 2(c). The value of $g^{(2)}(x = 0)$ was obtained through a Gaussian fit and calculated to be 1.007, much less than that of visible pseudo-thermal light generated with a laser and ground glass plate. The reason for this is complex, but the main cause is the low absorption of the SiC grains, which leads to low contrast of the speckles. Other factors are the characteristics of the source, sandpaper, and CCD. A large size and polychroism of the x-ray source will blur the edges of the images of the sandpaper grains, which will also reduce the value of $g^{(2)}$. Although 200 measurements are not enough for a good calibration, the fact that there is a correlation peak indicates that our pseudo-thermal x-ray source may be used to realize intensity correlation imaging. In addition, the 0.4 mm full width at half-maximum of the peak gives the resolution of the system.

Finally, the ghost image $G(x, y)$ was retrieved after N measurements by calculating the correlation using

$$G(x, y) = \langle SI(x, y) \rangle - \langle S \rangle \langle I(x, y) \rangle \\ \approx \frac{1}{N} \sum_{i=1}^N S_i I_i(x, y) - \frac{1}{N^2} \sum_{i=1}^N S_i \sum_{i=1}^N I_i(x, y), \quad (3)$$

where S is the integrated bucket detector intensity and $I(x, y)$ is the measured intensity at each pixel of CCD2.

The first object was a stainless steel mask ~ 5 mm in width as shown in Fig. 3(a), with the stenciled letters “CAS.” The bucket

detector was CCD1, same as the reference detector, but switched to 8×8 on-chip binning to save data transfer time. The exposure time for each frame was 150 ms. The XGI image after averaging over $N = 10^4$ shots is shown in Fig. 3(b). In practice, a real single-pixel bucket detector could have been used, which would also reduce costs, but for convenience we just used the same CCD1 and integrated the total intensity at the pixels.

To test XGI on a natural biological object, a small shell about 6 mm in length was chosen; see Fig. 3(c). A projection image taken by CCD1 is shown in Fig. 3(d) for comparison. For the XGI image, CCD1 was chosen as the bucket detector. Since the shell contains more detail, the exposure time for each frame was lengthened to 220 ms. The XGI image is shown in Fig. 3(e), again reconstructed from 10^4 measurements. It is obviously not as detailed as the projection image, since GI should be calculated by Eq. (3) where $\langle \dots \rangle$ denotes an infinite number of measurements, which of course is not possible. The more complex an object, the harder it is to obtain good-quality images and the more exposures are required. In Fig. 3(e) we may see that the contour is quite clear and the gray-scale regions contain rich information about the interior of the shell.

To reduce the radiation dose on the object we changed the bucket detector from CCD1 to CCD2, a direct imaging Princeton Instrument PIXIS-XB:1300 camera based on a 100 μm thick silicon chip, with resolution of 20 μm and quantum efficiency $\sim 50\%$. The object was the “CAS” mask, and the exposure for each frame was shortened by a factor of more than 10^5 to $t_0 = 1 \mu\text{s}$. The XGI image after averaging over $N = 10^4$ exposures is shown in Fig. 4(a). The total exposure time required for each image was $t = Nt_0 = 10$ ms. Figure 4(b) shows a projection image taken single-shot by CCD2 with the same exposure time of $t = 10$ ms; the image here is barely discernible. Even though a much longer time is required to make all the XGI measurements, the total exposure time would be only 10 ms. The actual radiation dose in our XGI experiment was quantified using an imaging plate (Fuji Film, SR2025) placed in the beam after the sandpaper; total flux was estimated to be $\sim 2.9 \times 10^5$ photons/s \cdot mm 2 [26]. This corresponds to 120 photons/s per pixel of CCD2. Since the accumulated exposure was 10 ms, the total number of x-ray photons required to obtain the XGI image was only 1.2 photons/pixel or, more precisely, 480 photons/unit resolution area of 0.4×0.4 mm 2 in our case. This is significant for biological organisms

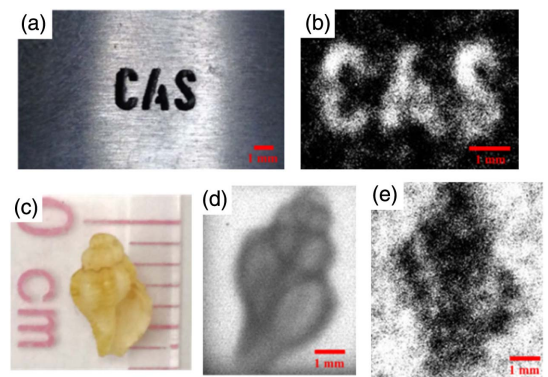


Fig. 3. Objects and images. (a) Photo of the “CAS.” (b) Ghost image of the “CAS” for $N = 10^4$ exposures. (c) Photo of the shell. (d) Projection x-ray image of the shell taken with CCD1 under 10 s exposure. (e) Ghost image of the shell for $N = 10^4$ exposures.

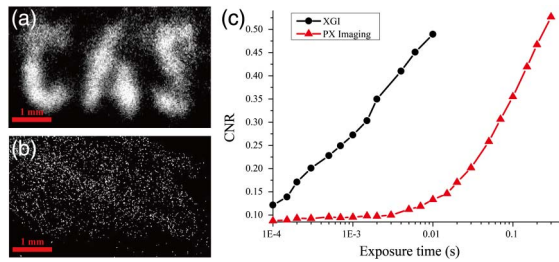


Fig. 4. Images obtained with CCD2. (a) XGI image for 10^4 frames and a total exposure time of 10 ms; the CNR is 0.5. (b) Projection x-ray image after an exposure of 10 ms; the CNR is 0.13. (c) CNR versus total exposure time.

when radiation damage is a concern. Of course, in practice we would need to shutter the beam before the object or use a pulsed source.

An important quantitative indicator of image quality is the contrast-to-noise ratio (CNR), defined as [27]

$$\text{CNR} \equiv \frac{\langle G_{\text{in}}(\vec{r}) \rangle - \langle G_{\text{out}}(\vec{r}) \rangle}{\sqrt{\sigma_{\text{in}}^2 + \sigma_{\text{out}}^2}}, \quad (4)$$

where G_{in} and G_{out} are the XGI signals for any point where the transmission is 1 or 0, respectively; σ_{in}^2 and σ_{out}^2 are the corresponding variances, i.e., $\sigma^2 \equiv \langle G^2(\vec{r}) \rangle - \langle G(\vec{r}) \rangle^2$. The CNR of the image in Fig. 4(a) is calculated to be 0.5, while that of Fig. 4(b) is just 0.1.

A plot of the CNR of XGI and projection imaging as a function of total exposure time is shown in Fig. 4(c). The abscissa corresponds to Nt_0 , and it should be noted that this axis is logarithmic. We see that for short exposure times, i.e., low radiation doses, the CNR of XGI (black circles) improves much more rapidly than that of projection imaging (red triangles).

It is important to note that the CNR of XGI can be different even for the same Nt_0 . For example, in the limiting case of $N = 1$ and $t_0 = 10$ ms, we only have one bucket signal, so obviously no ghost image would be obtainable and the CNR would be 0. Since the crucial issue is the total incident flux, we should optimize N and t_0 to obtain the best image for a given total exposure time. Figure 4(c) is not necessarily the optimal case, but for a given Nt_0 , XGI is better than projection imaging.

It may be observed that the edges of the letters in Fig. 4(a) appear somewhat blurred. This is because, as mentioned before, the resolution is determined by the speckle size of ~ 0.4 mm, which is determined by the SiC grain size. If finer sandpaper were used, the resolution would be higher and the edges clearer.

In conclusion, we have realized XGI using a tabletop x-ray source under ultra-low x-ray illumination. Real objects were imaged with a quality surpassing that of projection imaging for the same low flux with a lower-resolution camera. The setup is very simple, relatively inexpensive, and easy to operate. Pre-recording of the patterned illumination can be performed with a bright beam, while actual exposure of the object can be realized with a low-resolution camera or single-pixel detector under a dosage on the order of single photons per pixel. This is obviously an

important advantage in analysis of sensitive biological specimens. The spatial resolution could be improved with finer speckle patterns or various computational methods, while, by shortening the longitudinal coherence length, it should be possible to perform tomographical XGI.

Funding. National Key R&D Program of China (2017YFB0503300); National Natural Science Foundation of China (NSFC) (11334013, 11721404, 61675016); Chinese Academy of Sciences (CAS) (XDB17030500); Defense Industrial Technology Development Program (JCKY2016601C005).

[†]These two authors contributed equally to this work.

REFERENCES

1. R. Ballabriga, M. Campbell, and X. Llopart, Nucl. Instrum. Methods Phys. Res. A **878**, 10 (2018).
2. T. B. Pittman, Y. H. Shih, D. V. Strelakov, and A. V. Sergienko, Phys. Rev. A **52**, R3429 (1995).
3. D. Zhang, Y.-H. Zhai, L.-A. Wu, and X.-H. Chen, Opt. Lett. **30**, 2354 (2005).
4. J. H. Shapiro, Phys. Rev. A **78**, 61802 (2008).
5. Y. Bromberg, O. Katz, and Y. Silberberg, Phys. Rev. A **79**, 53840 (2009).
6. W. L. Chan, K. Charan, D. Takhar, K. F. Kelly, R. G. Baraniuk, and D. M. Mittleman, Appl. Phys. Lett. **93**, 121105 (2008).
7. P. Sen, B. Chen, G. Garg, S. R. Marschner, M. Horowitz, M. Levoy, and H. P. A. Lensch, ACM Trans. Graph. **24**, 745 (2005).
8. M. G. L. Gustafson, J. Microsc. **198**, 82 (2000).
9. J.-E. Oh, Y.-W. Cho, G. Scarcelli, and Y.-H. Kim, Opt. Lett. **38**, 682 (2013).
10. W. Yu, X. F. Liu, X. R. Yao, C. Wang, G. J. Zhai, and Q. Zhao, Phys. Lett. A **378**, 3406 (2014).
11. J. Cheng, Opt. Express **17**, 7916 (2009).
12. Y. Wu, P. Ye, I. O. Mirza, G. R. Arce, and D. W. Prather, Opt. Express **18**, 24565 (2010).
13. V. Studer, J. Bobin, M. Chahid, H. S. Mousavi, E. Candes, and M. Dahan, Proc. Natl. Acad. Sci. USA **109**, E1679 (2012).
14. W. K. Yu, X. R. Yao, X. F. Liu, R. M. Lan, L. A. Wu, G. J. Zhai, and Q. Zhao, Opt. Commun. **371**, 105 (2016).
15. B. Sun, M. P. Edgar, R. Bowman, L. E. Vittert, S. Welsh, A. Bowman, and M. J. Padgett, Science **340**, 844 (2013).
16. B. I. Erkmen and J. H. Shapiro, Adv. Opt. Photon. **2**, 405 (2010).
17. C. Zhao, W. Gong, M. Chen, E. Li, H. Wang, W. Xu, and S. Han, Appl. Phys. Lett. **101**, 141123 (2012).
18. H. Yu, R. Lu, S. Han, H. Xie, G. Du, T. Xiao, and D. Zhu, Phys. Rev. Lett. **117**, 113901 (2016).
19. D. Pelliccia, A. Rack, M. Scheel, V. Cantelli, and D. M. Paganin, Phys. Rev. Lett. **117**, 113902 (2016).
20. A. Schori and S. Schwartz, Opt. Express **25**, 14822 (2017).
21. R. I. Khakimov, B. M. Henson, D. K. Shin, S. S. Hodgman, R. G. Dall, K. G. H. Baldwin, and A. G. Truscott, Nature **540**, 100 (2016).
22. K. S. Morgan, D. M. Paganin, and K. K. W. Siu, Appl. Phys. Lett. **100**, 124102 (2012).
23. I. Zanette, T. Zhou, A. Burvall, U. Lundström, D. H. Larsson, M. Zdora, P. Thibault, F. Pfeiffer, and H. M. Hertz, Phys. Rev. Lett. **112**, 253903 (2014).
24. H. Wang, Y. Kashyap, and K. Sawhney, Sci. Rep. **6**, 20476 (2016).
25. M. C. Zdora, P. Thibault, F. Pfeiffer, and I. Zanette, J. Appl. Phys. **118**, 113105 (2015).
26. B. R. Maddox, H. S. Park, B. A. Remington, N. Izumi, S. Chen, C. Chen, G. Kimminau, Z. Ali, M. J. Haugh, and Q. Ma, Rev. Sci. Instrum. **82**, 23111 (2011).
27. P. Zerom, Z. Shi, M. N. O'Sullivan, K. W. C. Chan, M. Krogstad, J. H. Shapiro, and R. W. Boyd, Phys. Rev. A **86**, 63817 (2012).